Journal of Asian Earth Sciences 152 (2018) 80–90

Contents lists available at ScienceDirect

Journal of Asian Earth Sciences

journal homepage: www.elsevier.com/locate/jseaes

Full length article

Basal accretion, a major mechanism for mountain building in Taiwan revealed in rock thermal history

Chih-Tung Chen[a,b,*], Yu-Chang Chan[c], Ching-Hua Lo[b], Jacques Malavieille[d,f], Chia-Yu Lu[b,f], Jui-Ting Tang[b], Yuan-Hsi Lee[e]

[a] Department of Earth Sciences, National Central University, No. 300, Zhongda Road, Zhongli, Taiwan, ROC
[b] Department of Geosciences, National Taiwan University, No. 1, Sec. 4, Roosevelt Road, Taipei, Taiwan, ROC
[c] Institute of Earth Sciences, Academia Sinica, No. 128, Sec. 2, Academia Road, Nangang, Taipei, Taiwan, ROC
[d] Université de Montpellier, Géosciences Montpellier, Place E. Bataillon, 34095 Montpellier Cedex 5, France
[e] Department of Earth and Environmental Sciences, National Chung Cheng University, No. 168, University Road, Min-Hsiung, Chiayi, Taiwan, ROC
[f] LIA D3E, C.N.R.S.-M.O.S.T. France-Taiwan International Laboratory, France, Taiwan, ROC

ARTICLE INFO

Keywords:
Basal accretion
Time-temperature history
Mountain root
Orogenic wedge
Taiwan mountain belt

ABSTRACT

Deep tectonic processes are key integral components in the evolution of mountain belts, while observations of their temporal development are generally obscured by thermal resetting, retrograde alteration and structural overprinting. Here we recorded an integrated rock time-temperature history for the first time in the pro-wedge part of the active Taiwan arc-continent collision starting from sedimentation through cleavage-forming state to its final exhumation. The integrated thermal and age results from the Raman Spectroscopy of Carbonaceous Material (RSCM) method, zircon U-Pb laser ablation dating, and *in-situ* $^{40}Ar/^{39}Ar$ laser microprobe dating suggest that the basal accretion process was crucial to the development of the Taiwanese orogenic wedge. The basal accretion process commenced early in the mountain building history (~6 Ma) and gradually migrated to greater depths, as constrained by persistent plate convergence and cleavage formation under nearly isothermal state at similar depths until ~ 2.5 Ma recorded in the early-accreted units. Such development essentially contributed to mountain root growth by the increased depth of the wedge detachment and the downward wedge thickening during the incipient to full collision stages in the Taiwan mountain belt.

1. Introduction and tectonic background

Records of the depth-temperature-time trajectory of rocks through orogens are crucial in understanding the thermal-kinematic evolution of mountain belts (Huerta et al., 1999; Konstantinovskaia and Malavieille, 2005). In addition, knowledge on the coupling between tectonic and surface processes allows a better analysis of this evolution (e.g., Malavieille, 2010), particularly on exhumation mechanisms. Recent advances in low-temperature thermochronology and seismic imaging provided high-resolution insights into the exhumation and the current state of mountain building processes, respectively (e.g. Fuller et al., 2006; Lee et al., 2015; Wu et al., 2014; Huang et al., 2015). In contrast, the kinematics along the prograde metamorphic trajectory is beyond the reaches of afore-mentioned techniques; constraints from metamorphic mineral assemblages are easily obscured by retrograde reactions, except where retained in inclusions of garnet and other chemically-robust minerals (e.g. King et al., 2004). Such information on thermal history and kinematics, central to deciphering processes including wedge accretion and mountain root growth (Glodny et al., 2005; Malavieille, 2010), are therefore often missing for orogens outcropping only medium- to low-grade metamorphic rocks. The active arc-continent collision in Taiwan (Malavieille et al., 2002; Byrne et al., 2011), exposing intermediate-grade rocks in its core and hinterland (Ernst and Jahn, 1987), serves as a reference model in such investigations.

The island of Taiwan results from the active convergence between the Eurasian and Philippine Sea plates, where the ongoing oblique collision between the Chinese continental margin and the Luzon Arc following the subduction of the South China Sea along the Manila Trench leads to the southward propagation of the orogen (Suppe, 1984; Fig. 1A). Due to the subtropical climate, surface processes are particularly efficient and Taiwan Island represents an ideal natural laboratory to observe and study mountain building. Moreover, distinct spatial-temporal relationship in orogenic evolution offers insights into the various processes operating alive at different stages of mountain building simultaneously (Teng, 1990). Southern to central Taiwan is in

* Corresponding author at: Department of Earth Sciences, National Central University, No. 300, Zhongda Road, Zhongli, Taoyuan City 32001, Taiwan, ROC.
E-mail addresses: kthomasch@gmail.com, chihtung@ncu.edu.tw (C.-T. Chen).

https://doi.org/10.1016/j.jseaes.2017.11.030
Received 31 May 2017; Received in revised form 19 November 2017; Accepted 22 November 2017
Available online 22 November 2017
1367-9120/

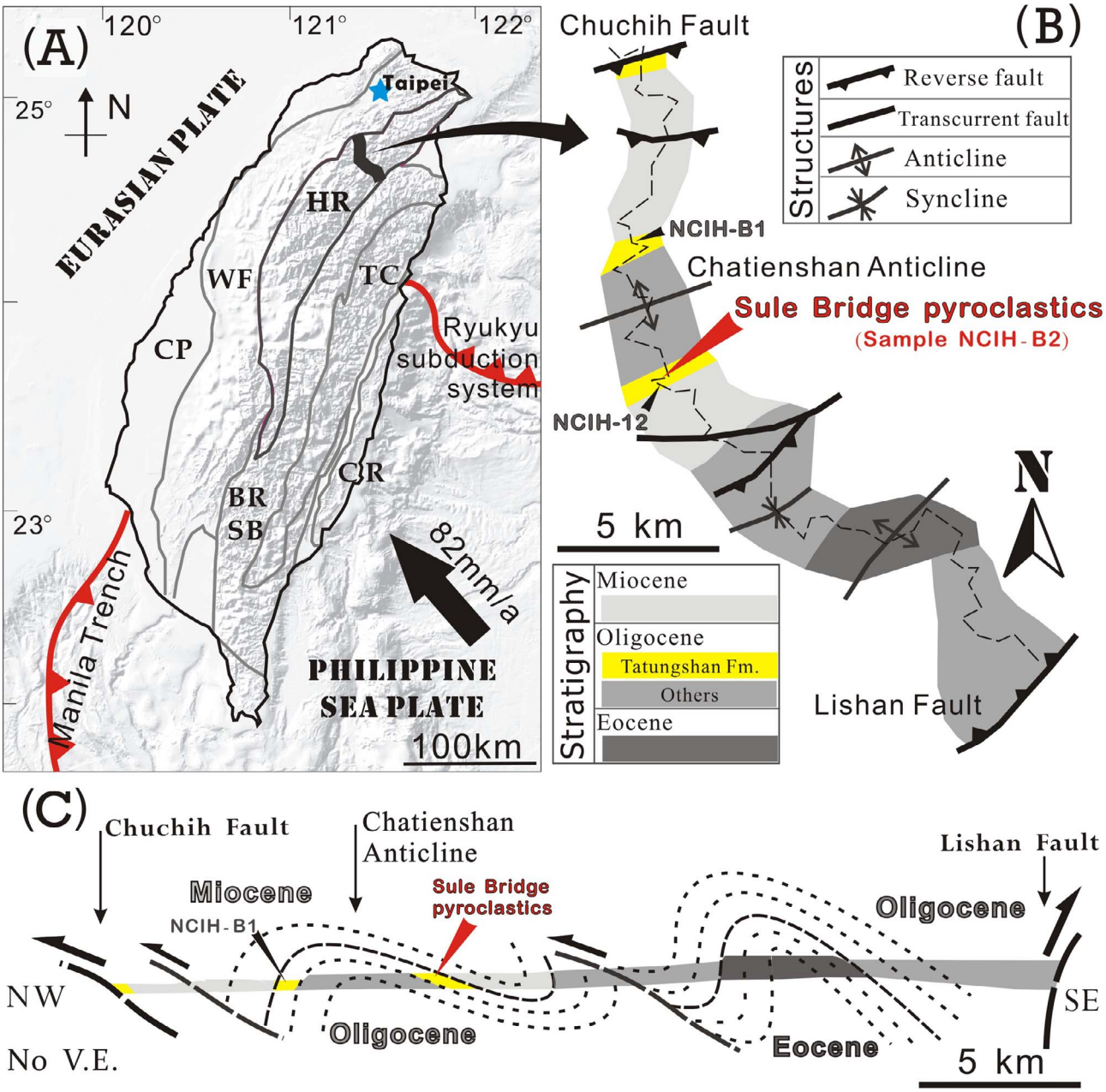

Fig. 1. (A) Outline of major tectonic units in Taiwan. CP: Coastal Plain; WF: Western Foothills; HR: Hsuehshan Range; BRSB: Backbone Range Slate Belt; TC: Tananao Schist Complex; CR: Coastal Range. The black strip in the HR area marks the vicinity of the North Cross Island Highway. (B) Geologic strip map along the North Cross Island Highway, with outcrop and sample locations marked. (C) Geologic cross section of the area oriented NW-SE.

the incipient to full collision stages with rapid shortening and rock uplift rates (Shyu et al., 2005; Fuller et al., 2006); while the mountain building is complete, and collision ceased with commencing post-orogenic collapse in northern Taiwan (Wu et al., 2009; Chen et al., 2014). The onset of the collision is constrained at ~6.5 Ma based on records in both the foreland and intra-arc basins (Chi et al., 1981; Lin et al., 2003), or inferred from rapid exhumation since ~3 Ma (Liu et al., 2001; Lee et al., 2015; Hsu et al., 2016). The timing of rock deformation and metamorphism associated with the current orogeny, in contrast, remains unresolved due to the scarcity of relevant datable materials in the rocks of the Central Range, the metamorphic core of Taiwan.

For the Tananao Schist Complex, the exhumed Chinese continental margin basement, the late Cenozoic orogeny has peak metamorphic conditions above the closure temperatures of the K-Ar system for the foliation-defining minerals including K-feldspar, biotite, and muscovite (Lo and Onstott, 1995; Beyssac et al., 2007). The presence of an older orogeny, the Mesozoic Nanao Event resulted from paleo-Pacific subduction, further complicates the metamorphic records (Yui et al., 1988). The only reliable dating of deformational fabrics within the Tananao complex was the 4.1–3.0 Ma mylonitization from $^{40}Ar/^{39}Ar$ dating of biotite extracts, while the related thrust shearing was believed to have taken place during retrograde conditions (Wang et al., 1998). As a result, the history from the prograde to peak conditions is ambiguous for the Tananao rocks. Promising alternatives may exist in the rest of the Central Range, particularly the Hsuehshan Range slate belt (Fig. 1A) whose mainly Paleogene continental margin sediments were deformed and metamorphosed exclusively during the late Cenozoic Taiwan Orogeny (Teng, 1992).

The Hsuehshan Range consists of meta-sediments originated from eastward-deepening grabens on the outer part of the Chinese continental margin (Teng, 1990). The margin was sub-aerial prior to Eocene, then the grabens were formed in response to rifting associated

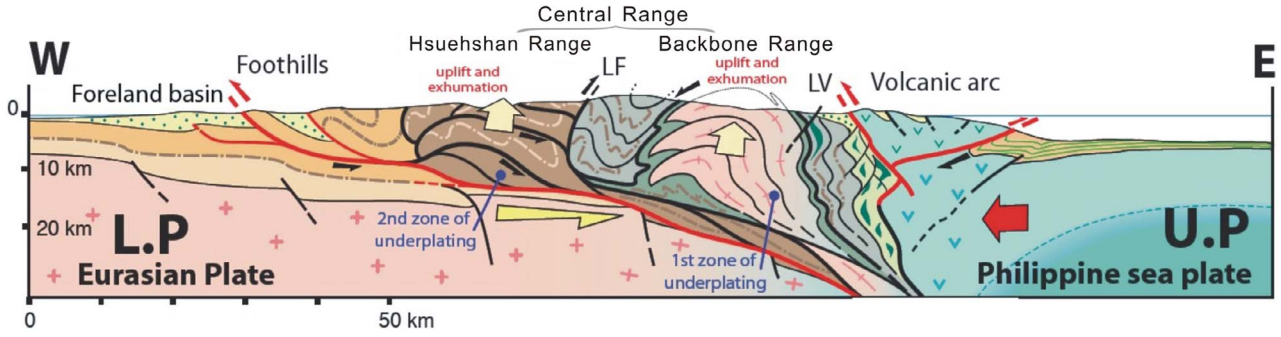

Fig. 2. Schematic section across the orogenic wedge of Taiwan. It shows the setting of the Hsuehshan Range and its tectonic relationships with neighboring tectonic units. LF: Lishan Fault; LV: Longitudinal Valley.

with the opening of the South China Sea. The grabens were active until late Oligocene, and were simultaneously filled up forming sediment wedges 10 km-thick or more (Lin et al., 2003). Margin-wide thermal subsidence led Miocene shelf series to drape atop the grabens before the Neogene Taiwan Orogen encroached on the continental margin (Teng and Lin, 2004). The entire range now resembles a large-scale pop-up structure on the pro-wedge side of the orogen (Fig. 2), buttressing against the Western Foothills to the west along the Chuchih Thrust and juxtaposed to the Backbone Range slate belt to the east by the back-thrust Lishan Fault (Clark et al., 1993; Lee et al., 1997; Brown et al., 2012). Magnitude of metamorphism and exhumation increases eastward within the range, and the rocks are metamorphosed to prehnite-pumpellyite grade with a greenschist-facies core in the east (Liou and Ernst, 1984). Thermal-metamorphic investigations revealed that the northern and the central-southern parts of the range were characterized by contrasting thermal histories and were derived from different portions of the graben system (Chen et al., 2011). The south-central part of the Hsuehshan Range, initially from distal portions of the graben system on the continental margin, was frontal-accreted into the orogenic wedge and transported towards the foreland, thus possessing mainly static diagenetic metamorphism (Beyssac et al., 2007). The northern counterpart instead, was drawn from more proximal portions of the margin and exhibits prominent dynamic synorogenic metamorphism overprint, signifying underthrusting and basal-accretion before exhumation (Chen et al., 2011). The northern part of the Hsuehshan Range is therefore well-suited for investigating the prograde evolution of Taiwanese mountain building. However, the minute sizes of newly-grown micas in slate under prehnite to lower-greenschist grade prevent conclusive dating results with possible detrital contamination. A layer of mafic pyroclastics within late Oligocene slate succession in the northern Hsuehshan Range (Yang and Shau, 1988) presents a unique opportunity as millimetre-scale syn-kinematic mica porphyroblasts are found growing along spaced pressure solution seams (Chen et al., 2016; Fig. 4A, B), allowing utilization of *in-situ* $^{40}Ar/^{39}Ar$ laser microprobe age results (Chen et al., 2016) in tandem with mineralogical and structural controls to pinpoint the timing and conditions of metamorphic foliation formation (Chan et al., 2000).

In the following, multiple petrologic and chronological methods are utilized to constrain the time-temperature history of the particular meta-pyroclastics, the Sule Bridge pyroclastics (NCIH-B2), during the late-Cenozoic Taiwan Orogeny. By integration into regional structural framework, the kinematics of basal accretion and resultant mountain root growth under the pro-wedge are elucidated, which lead to significant reappraisal of mountain building processes in Taiwan.

2. Thermal and chronologic constraints

2.1. The Sule Bridge pyroclasticse

The metamorphosed mafic Sule Bridge pyroclastics outcrops along the Northern Cross Island Highway which traverses the northern part of the Hsuehshan Range (Fig. 1B). The pyroclastics lies conformably within the sedimentary succession belonging to the Tatungshan Formation of late Oligocene time (Chang, 1973; Teng, 1992). The site is positioned on the eastern limb of the Chatienshan Anticline, with local beddings strike northeast and dip moderately to the southeast (Fig. 1B and C). Cleavage in neighboring slate shows similar attitude as the beddings but with steeper dip. Continuous foliation (slaty cleavage) did not form in the pyroclastics and spaced pressure solution seams with the same attitude were developed instead. On those ~1 cm-apart spaced foliation defined by pressure solution planes, numerous mica porphyroblasts containing chloritic minerals or albite are found along and parallel to the foliation, demonstrating their syn-tectonic origin (Chen et al., 2016; Fig. 4A, B). As demonstrated by the shapes and texture of the porphyroblasts as well as features around the pressure solution seams, formation of foliation within the Sule Bridge pyroclastics was mainly through pure shear deformation (Chen et al., 2016). Maximum burying temperature of about 300 °C was suggested by nearby vitrinite reflectance data (Chen et al., 2011), far lower than the closure temperature for K-Ar system of muscovite (~490 °C; Harrison et al., 2009). Such exceptional circumstance combining large syn-kinematic mica growth with rather low peak metamorphic condition offers a good opportunity to date cleavage directly (Chan et al., 2000). In order to construct the first complete time-temperature path of Taiwanese metamorphic rock, whole rock chemistry (Table 1), zircon U-Pb dating, and Raman spectroscopy of carbonaceous material (RSCM) are carried out and complemented by published *in-situ* $^{40}Ar/^{39}Ar$ laser microprobe dating results (Chen et al., 2016) and apatite fission-track (FT) data (Wang, 2011).

2.2. Analytical methods

2.2.1. RSCM (Raman Spectroscopy of Carbonaceous Material)

Slate of a nearby sample (NCIH-12; Fig. 1) was cut perpendicular to the slaty cleavage and then processed to polished thin sections. Raman spectra were obtained using a Renishaw inVia microspectrometer equipped with a 514-mm argon laser housed in Tatung University, Taipei, Taiwan. The laser was focused on the sample using a DMLM Leica microscope with a 50× objective, and the laser power at the sample surface was set at around 1 mW. The signal was filtered by edge filters and finally dispersed using an 1800 gr/mm grating to be analyzed by a Peltier cooled CCD detector. Before each session, the spectrometer was calibrated using a silicon standard. Analytical and fitting procedures described by Beyssac et al. (2002) were strictly followed to avoid analytical pitfalls. 14 spectra were measured in the extended scanning mode (1000–2000 cm^{-1}) with acquisition times from 10 to 30 s. Spectra were then processed using the software Peakfit following Beyssac et al. (2003). The result is presented in Table 2.

Table 1
Chemical compositions of samples NCIH-B2 and B1.

Sample	NCIH-B2	NCIH-B1
Locality		
Lat. (°)	24.70157	24.75295
Lon. (°)	121.35822	121.34942
Oxides (wt.%)		
SiO_2	48.59	40.99
TiO_2	2.36	3.90
Al_2O_3	15.14	17.11
Fe_2O_3	12.23	12.62
MnO	0.08	0.17
MgO	5.87	7.62
CaO	4.36	6.13
Na_2O	2.19	1.79
K_2O	1.47	1.82
P_2O_5	0.15	0.83
Total	92.43	92.98
Element (ppm)		
V	166	258
Cr	279	57
Co	38	38
Ni	216	78
Cu	94	33
Zn	101	78
Ga	22	22
Rb	66.0	78.1
Sr	221	623
Y	24	34
Zr	199	470
Nb	22.6	116.8
Cs	4.0	6.3
Ba	216	787
La	16.9	72.0
Ce	34.2	145.2
Pr	3.9	17.1
Nd	15.7	64.1
Sm	4.0	11.6
Eu	1.12	3.47
Gd	4.24	9.04
Tb	0.67	1.23
Dy	4.24	6.83
Ho	0.89	1.31
Er	2.38	3.30
Tm	0.35	0.45
Yb	2.17	2.86
Lu	0.32	0.41
Hf	4.89	9.26
Ta	1.44	7.50
W	1.05	1.19
Tl	0.7	1.0
Pb	8.9	5.3
Th	5.1	9.1
U	1.23	2.36

Table 2
RSCM temperature measurement result. See Beyssac et al. (2002) and Lahfid et al. (2010) for more details.

Sample	Lat. (°)	Lon. (°)	Spectra	RA1 ratio	T_{MAX} (°C)	sd (°C)
NCIH-12	24.69983	121.36050	14	0.57	246	5

2.2.2. Zircon U-Pb laser ablation dating

Zircons were separated from ~10 kg rock samples of the Sule Bridge pyroclastics and NCIH-B1 (the same mafic pyroclastic outcropping on the western limb of the Chatienshan Anticline; Fig. 1) using conventional heavy-liquid and magnetic separation techniques. Zircon U-Pb analyses were carried out using laser ablation-inductively coupled plasma mass spectrometry (LA-ICP-MS) housed at the Department of Geosciences, National Taiwan University, Taipei, where Agilent 7500s quadrupole ICP-MS is attached with a New Wave UP213 laser ablation system. The analytical procedures were detailed in Chiu et al. (2009). The results are given in Table 3.

2.3. Results

Concerning the protolith characteristics of the pyroclastics revealed in whole-rock chemistry (Table 1), the Sule Bridge pyroclastics is mafic, and the rare-earth element patterns resemble the Kungkuan alkali basalts of northern Taiwan (Chung et al., 1994; Wang et al., 2012). Deposition age of the pyroclastics inferred by zircon U-Pb dates, which may result from either detrital mixing during transport-sedimentation or crystallization from parental magma, is no older than 24 Ma (the youngest obtained date; Fig. 3; Table 3). The deposition age is consistent with the strata age of latest Oligocene, which suggests little basin burial for the mafic pyroclastics as the overlying Miocene strata are less than 2 km thick (Teng, 1992). RSCM result from the nearby slate sample NCIH-12, which reflects the peak temperature of the rock, is 246 ± 5 °C (Table 2) and therefore suggests tectonic metamorphic overprint through underthrusting during basal accretion (Glodny et al., 2005; Chen et al., 2011).

To pin down the age of cleavage formation, a thick section of the Sule Bridge pyroclastics containing one major pressure solution seam (Fig. 4B) was prepared following Chan et al. (2000) for *in-situ* $^{40}Ar/^{39}Ar$ laser microprobe dating. At least three mica porphyroblasts are found along the seam and are composed of muscovite with minor corrensite, a potassium-bearing chloritic mineral formed by alteration of basic igneous rocks and reported in this particular pyroclastics (Shau et al., 1990). Corrensite may be directly derived from alteration of the pyroclastic body, while muscovite was likely originated from neighboring sedimentary strata due to the mafic content of the Sule Bridge pyroclastics. Both minerals are stacked and intercalated parallel to the foliation demonstrating the syn-kinematic and co-genetic nature of their growth (Fig. 4A and B; Chen et al., 2016). Isotopic composition of Ar gases is extracted by using *in-situ* $^{40}Ar/^{39}Ar$ laser microprobe analyses which create pits of tens of microns, allowing high spatial resolution of ages within the porphyroblasts. In total 120 and 5 spot-fusion analyses are performed on muscovite and corrensite fabrics, respectively (Chen et al., 2016; Fig. 4C). The muscovite results are distributed over a rather long time span, from 6.2 to 2.3 Ma with a mean age of 4.6 Ma; the corrensite results are also dispersed between 2.5 and 5 Ma (Fig. 4D; Chen et al., 2016). The results represent the growth ages of the analyzed mineral fibers, since the peak temperature of the sample (246 ± 5 °C) was markedly lower than the resetting temperature of muscovite (~490 °C) as previously noted (Harrison et al., 2009). The distribution of ages is not organized as commonly anticipated for mica fish and related strain shadow microstructures with an initial core flanked by outward growth, or vice versa (Passchier and Trouw, 2005); instead a random distribution is observed (Fig. 4C) as resulted from brittle micro-boudinage and crack-seal (Chen et al., 2016). To summarize, the mica porphyroblasts and the host pressure solution seam were developed during 6.3 to 2.3 Ma in a fairly continuous manner (Chen et al., 2016).

Following cleavage formation, the retrograde cooling in thermal-kinematic history could be constrained by apatite fission-track dating, since the peak metamorphic temperature was lower than the reset temperature of zircon FT and produces partial-reset ages in the area (Liu et al., 2001). Apatite FT result from a nearby meta-sandstone is 1.6 ± 0.3 Ma (Wang, 2011), suggesting rapid exhumation consistent with orogen-wide trend (Lee et al., 2015).

3. Time-temperature evolution

The complete record from sedimentation, peak metamorphic state, cleavage formation, and exhumation outlined above presents a full thermal history of Taiwanese metamorphic rocks for the first time (Fig. 5A). The Sule Bridge pyroclastics was deposited as a volcaniclastic

Table 3
Results of Zircon U-Pb laser ablation dating on samples NCIH-B2 and B1.

Spot	U (ppm)	Th/U	U-Th-Pb ratios								Ages (Ma)						Inferred age (Ma)	1σ
			206Pb/238U	1σ	207Pb/206Pb	1σ	207Pb/235U	1σ	208Pb/232Th	1σ	206Pb/238U	1σ	207Pb/206Pb	1σ	207Pb/235U	1σ		
NCIH-B2 results																		
B2-01	94	0.735	0.16149	0.00363	0.08195	0.00104	1.82468	0.05159	0.03266	0.00097	965	20	1244	23	1054	19	965	20
B2-02	200	0.709	0.04115	0.00096	0.06948	0.00117	0.39425	0.01356	0.00965	0.00031	260	6	913	32	337	10	260	6
B2-03	441	0.699	0.10988	0.00214	0.07095	0.00068	1.07475	0.02351	0.03526	0.00101	672	12	956	18	741	12	672	12
B2-04	346	0.943	0.02553	0.00060	0.10488	0.00152	0.36921	0.01159	0.00641	0.00022	163	4	1712	24	319	9	163	4
B2-05	1376	0.295	0.03873	0.00082	0.06890	0.00072	0.36787	0.00880	0.01193	0.00035	245	5	896	20	318	7	245	5
B2-06	1034	1.351	0.01732	0.00034	0.08481	0.00079	0.20249	0.00431	0.00543	0.00013	111	2	1311	17	187	4	111	2
B2-07	437	0.227	0.14089	0.00272	0.07575	0.00068	1.47134	0.03004	0.03868	0.00094	850	15	1088	16	919	12	850	15
B2-08	452	1.075	0.03601	0.00082	0.07163	0.00416	0.35567	0.02704	0.01090	0.00020	228	5	975	110	309	20	228	5
B2-09	493	0.437	0.03309	0.00071	0.05686	0.00263	0.25939	0.01612	0.01028	0.00019	210	4	486	95	234	13	210	4
B2-10	324	1.176	0.10928	0.00206	0.07980	0.00079	1.20232	0.02700	0.02971	0.00107	669	12	1192	18	802	12	669	12
B2-11	529	0.741	0.00473	0.00013	0.08525	0.00654	0.05560	0.00552	0.00140	0.00003	30.4	0.9	1321	139	55	5	30.4	0.9
B2-12	1344	0.295	0.03336	0.00069	0.05252	0.00172	0.24161	0.01150	0.01047	0.00019	212	4	308	69	220	9	212	4
B2-13	266	1.031	0.02009	0.00049	0.07463	0.00465	0.20675	0.01707	0.00605	0.00012	128	3	1059	117	191	14	128	3
B2-14	194	0.181	0.03625	0.00146	0.09548	0.02256	0.47722	0.12906	0.01064	0.00272	230	9	1538	450	396	89	230	9
B2-15	348	0.909	0.02093	0.00043	0.07000	0.00076	0.20198	0.00496	0.00622	0.00013	134	3	928	20	187	4	134	3
B2-16	193	0.588	0.05309	0.00121	0.06499	0.00277	0.47569	0.02902	0.01624	0.00032	333	7	774	83	395	20	333	7
B2-17	266	0.704	0.01633	0.00037	0.06625	0.00116	0.14920	0.00520	0.00511	0.00015	104	2	814	34	141	5	104	2
B2-18	451	1.563	0.02019	0.00052	0.07683	0.00646	0.21391	0.02259	0.00606	0.00011	129	3	1117	157	197	19	129	3
B2-19	264	0.625	0.26351	0.00561	0.11861	0.00120	4.30919	0.09970	0.05905	0.00168	1508	29	1935	17	1695	19	1935	17
B2-20	448	0.709	0.39514	0.00772	0.13493	0.00120	7.35038	0.14772	0.10009	0.00220	2147	36	2163	14	2155	18	2163	14
B2-21	275	0.543	0.02825	0.00056	0.05238	0.00057	0.20399	0.00499	0.00808	0.00019	180	4	302	23	188	4	180	4
B2-21.1	225	0.503	0.02924	0.00063	0.05549	0.00253	0.22375	0.01392	0.00912	0.00016	186	4	432	94	205	12	186	4
B2-22	424	0.288	0.36524	0.00715	0.12611	0.00113	6.35001	0.12894	0.09768	0.00226	2007	34	2044	14	2025	18	2044	14
B2-23	289	0.398	0.11275	0.00236	0.07955	0.00157	1.23677	0.04516	0.03373	0.00066	689	14	1186	36	817	20	689	14
B2-24	488	0.243	0.16317	0.00347	0.07036	0.00072	1.58286	0.03738	0.03808	0.00116	974	19	939	19	963	15	974	19
B2-25	357	0.813	0.05144	0.00102	0.08720	0.00083	0.61846	0.01350	0.01451	0.00031	323	6	1365	17	489	8	323	6
B2-26	329	1.000	0.01837	0.00041	0.05246	0.00414	0.13285	0.01280	0.00576	0.00009	117	3	306	154	127	11	117	3
B2-27	1300	0.155	0.32814	0.00675	0.11739	0.00111	5.31072	0.11470	0.07592	0.00186	1829	33	1917	15	1871	18	1917	15
B2-28	297	0.840	0.02561	0.00053	0.07335	0.00388	0.25898	0.01800	0.00773	0.00013	163	3	1024	93	234	15	163	3
B2-29	461	1.136	0.00531	0.00012	0.10802	0.00205	0.07903	0.00289	0.00167	0.00006	34.1	0.8	1766	30	77	3	34.1	0.8
B2-30	1273	0.847	0.02026	0.00038	0.08106	0.00073	0.22641	0.00466	0.00632	0.00016	129	2	1223	15	207	4	129	2
B2-31	799	0.444	0.03310	0.00063	0.05610	0.00051	0.25600	0.00530	0.00990	0.00022	210	4	456	17	231	4	210	4
B2-32	1814	0.556	0.01715	0.00034	0.06373	0.00239	0.15073	0.00792	0.00526	0.00009	110	2	733	69	143	7	110	2
B2-33	2316	0.047	0.30616	0.00614	0.11337	0.00106	4.78505	0.10242	0.05313	0.00145	1722	30	1854	15	1782	18	1854	15
B2-34	147	1.471	0.02374	0.00072	0.15002	0.01149	0.49107	0.05063	0.00666	0.00017	151	5	2346	114	406	34	151	5
B2-35	584	0.521	0.04814	0.00096	0.06968	0.00275	0.46251	0.02502	0.01461	0.00026	303	6	919	70	386	17	303	6
B2-36	1204	0.474	0.02727	0.00051	0.06700	0.00228	0.25189	0.01207	0.00831	0.00014	173	3	838	61	228	10	173	3
B2-37	667	0.230	0.45287	0.00897	0.15911	0.00142	9.93583	0.19846	0.08504	0.00161	2408	40	2446	13	2429	18	2446	13
B2-38	269	0.617	0.07821	0.00154	0.07532	0.00071	0.81223	0.01762	0.02292	0.00053	485	9	1077	17	604	10	485	9
B2-39	1165	0.172	0.26980	0.00514	0.10004	0.00086	3.72119	0.07172	0.06503	0.00121	1540	26	1625	14	1576	15	1625	14
B2-40	254	0.725	0.03027	0.00063	0.06874	0.00340	0.28693	0.01888	0.00921	0.00016	192	4	891	89	256	15	192	4
B2-41	680	1.563	0.02527	0.00066	0.12488	0.00779	0.43504	0.03689	0.00721	0.00016	161	4	2027	96	367	26	161	4
B2-42	923	0.037	0.03451	0.00061	0.05009	0.00055	0.23838	0.00536	0.01089	0.00023	219	4	199	22	217	4	219	4
B2-44	288	0.422	0.04313	0.00086	0.05726	0.00061	0.34049	0.00823	0.01282	0.00034	272	5	502	20	298	6	272	5
B2-45	267	0.602	0.45297	0.00908	0.16535	0.00153	10.32696	0.21843	0.10082	0.00261	2408	40	2511	14	2465	20	2511	14
B2-46	321	0.885	0.01946	0.00038	0.06625	0.00070	0.17775	0.00423	0.00537	0.00013	124	2	814	19	166	4	124	2
B2-47	447	0.559	0.25055	0.00518	0.09827	0.00099	3.39505	0.07826	0.04317	0.00139	1441	27	1592	16	1503	18	1592	16
B2-48	134	1.163	0.12522	0.00253	0.06840	0.00070	1.18082	0.02764	0.03396	0.00096	761	14	881	18	792	13	761	14
B2-49	122	1.852	0.01662	0.00076	0.12734	0.02171	0.29176	0.06177	0.00473	0.00015	106	5	2062	263	260	49	106	5
B2-50	201	0.500	0.30324	0.00608	0.10441	0.00096	4.36495	0.09104	0.07505	0.00164	1707	30	1704	15	1706	17	1704	15
B2-51	700	1.389	0.08618	0.00169	0.07748	0.00072	0.92068	0.01957	0.01299	0.00034	533	10	1134	16	663	10	533	10

(*continued on next page*)

Table 3 (*continued*)

Spot	U (ppm)	Th/U	U-Th-Pb ratios								Ages (Ma)						Inferred age (Ma)	1σ
			206Pb/238U	1σ	207Pb/206Pb	1σ	207Pb/235U	1σ	208Pb/232Th	1σ	206Pb/238U	1σ	207Pb/206Pb	1σ	207Pb/235U	1σ		
B2-52	1681	0.115	0.35069	0.00636	0.15633	0.00135	7.55825	0.14908	0.08788	0.00251	1938	30	2416	13	2180	18	2416	13
B2-54	100	2.128	0.38257	0.00715	0.13214	0.00114	6.96952	0.13762	0.10855	0.00257	2088	33	2127	13	2108	18	2127	13
B2-55	515	0.658	0.05693	0.00108	0.08762	0.00077	0.68772	0.01384	0.01674	0.00038	357	7	1374	15	531	8	357	7
B2-56	430	1.163	0.04443	0.00083	0.05961	0.00056	0.36515	0.00780	0.01325	0.00033	280	5	589	18	316	6	280	5
B2-57	328	0.388	0.31217	0.00601	0.10967	0.00099	4.71998	0.09768	0.08609	0.00240	1751	30	1794	14	1771	17	1794	14
B2-58	441	1.786	0.01737	0.00051	0.08939	0.01203	0.21411	0.03426	0.00513	0.00010	111	3	1413	222	197	29	111	3
B2-60	135	0.518	0.14156	0.00278	0.07032	0.00068	1.37240	0.03026	0.04158	0.00114	853	16	938	17	877	13	853	16
B2-61	312	1.493	0.01886	0.00048	0.12394	0.00581	0.32231	0.02217	0.00539	0.00012	120	3	2014	72	284	17	120	3
B2-62	345	1.124	0.00553	0.00034	0.23667	0.03162	0.18040	0.03393	0.00148	0.00015	36	2	3098	188	168	29	36	2
B2-63	461	0.325	0.02658	0.00050	0.05441	0.00133	0.19936	0.00780	0.00830	0.00014	169	3	388	48	185	7	169	3
B2-65	366	0.270	0.34265	0.00652	0.11470	0.00099	5.41827	0.10638	0.09197	0.00200	1899	31	1875	14	1888	17	1875	14
B2-66	136	0.952	0.02384	0.00054	0.06064	0.00139	0.19931	0.00820	0.00666	0.00022	152	3	627	43	185	7	152	3
B2-67	463	0.725	0.32993	0.00628	0.11269	0.00098	5.12583	0.10124	0.09129	0.00210	1838	30	1843	14	1840	17	1843	14
B2-68	119	0.714	0.01604	0.00040	0.05698	0.00566	0.12602	0.01500	0.00498	0.00009	103	3	491	188	121	14	103	3
B2-69	708	1.163	0.01527	0.00030	0.06518	0.00063	0.13725	0.00306	0.00419	0.00010	98	2	780	18	131	3	98	2
B2-71	490	0.862	0.04414	0.00092	0.05738	0.00067	0.34918	0.00912	0.01291	0.00047	278	6	506	22	304	7	278	6
B2-71.1	696	0.735	0.04252	0.00092	0.06011	0.00073	0.35243	0.00955	0.01081	0.00040	268	6	608	23	307	7	268	6
B2-71.2	711	0.980	0.04187	0.00081	0.06385	0.00060	0.36863	0.00792	0.01278	0.00034	264	5	737	17	319	6	264	5
B2-72	182	1.010	0.07529	0.00152	0.06634	0.00072	0.68863	0.01680	0.02382	0.00075	468	9	817	20	532	10	468	9
B2-73	686	0.833	0.42159	0.00803	0.14969	0.00129	8.70061	0.16939	0.11548	0.00234	2268	36	2342	13	2307	18	2342	13
B2-74	167	0.680	0.00485	0.00013	0.06461	0.00656	0.04317	0.00537	0.00148	0.00003	31.2	0.8	762	185	43	5	31.2	0.8
B2-76	732	0.971	0.00433	0.00011	0.09892	0.00785	0.05906	0.00593	0.00127	0.00003	27.9	0.7	1604	128	58	6	27.9	0.7
B2-77	348	0.935	0.01861	0.00043	0.07120	0.00548	0.18266	0.01741	0.00564	0.00010	119	3	963	136	170	15	119	3
B2-78	494	0.813	0.01889	0.00037	0.05240	0.00053	0.13646	0.00316	0.00555	0.00012	121	2	303	20	130	3	121	2
B2-79	572	0.315	0.03412	0.00066	0.05044	0.00047	0.23729	0.00507	0.00972	0.00022	216	4	215	19	216	4	216	4
B2-80	249	0.342	0.04164	0.00081	0.05245	0.00053	0.30109	0.00690	0.01203	0.00028	263	5	305	20	267	5	263	5
B2-81	569	0.917	0.14951	0.00293	0.12445	0.00115	2.56541	0.05411	0.03995	0.00113	898	16	2021	14	1291	15	898	16
B2-82	2061	1.176	0.02313	0.00051	0.12457	0.00462	0.39730	0.02200	0.00661	0.00013	147	3	2023	57	340	16	147	3
B2-84	371	0.260	0.15441	0.00300	0.07257	0.00066	1.54491	0.03221	0.04259	0.00109	926	17	1002	16	948	13	926	17
B2-86	259	0.369	0.14210	0.00277	0.06982	0.00064	1.36807	0.02845	0.03762	0.00088	857	16	923	16	875	12	857	16
B2-87	711	0.151	0.15284	0.00306	0.07239	0.00067	1.52552	0.03249	0.04411	0.00114	917	17	997	16	941	13	917	17
B2-89	282	0.658	0.02280	0.00069	0.15915	0.01022	0.50021	0.04450	0.00635	0.00023	145	4	2447	94	412	30	145	4
B2-90	1375	0.347	0.01322	0.00049	0.12567	0.01967	0.22915	0.04320	0.00377	0.00044	85	3	2038	241	209	36	85	3
NCIH-B1 results																		
B1-1	239	0.495	0.03792	0.00075	0.06002	0.00066	0.31385	0.00773	0.01240	0.00036	240	5	604	22	277	6	240	5
B1-2	872	0.388	0.04913	0.00094	0.05681	0.00054	0.38486	0.00836	0.01583	0.00048	309	6	484	19	331	6	309	6
B1-03	427	0.690	0.07116	0.00137	0.07331	0.00066	0.71919	0.01483	0.02240	0.00047	443	8	1023	17	550	9	443	8
B1-04	196	0.490	0.28814	0.00551	0.10359	0.00091	4.11513	0.08213	0.08413	0.00181	1632	28	1689	15	1657	16	1689	15
B1-05	127	0.588	0.05032	0.00098	0.05414	0.00065	0.37563	0.00973	0.01600	0.00038	316	6	377	25	324	7	316	6
B1-06	395	0.143	0.07336	0.00141	0.05777	0.00052	0.58430	0.01216	0.02381	0.00055	456	8	521	18	467	8	456	8
B1-07	378	0.304	0.16453	0.00378	0.09025	0.00161	2.04735	0.07413	0.04856	0.00105	982	21	1431	31	1131	25	982	21
B1-08	283	0.746	0.00555	0.00014	0.05156	0.00355	0.03944	0.00356	0.00174	0.00003	35.7	0.9	266	144	39	3	35.7	0.9
B1-08-1	122	0.546	0.00602	0.00023	0.04926	0.00985	0.04089	0.00938	0.00190	0.00023	39	1	160	318	41	9	39	1
B1-08-2	207	0.595	0.00590	0.00027	0.07781	0.02058	0.06331	0.01925	0.00177	0.00013	38	2	1142	527	62	18	38	2
B1-09	476	0.617	0.03500	0.00257	0.20223	0.04329	0.97597	0.27659	0.00954	0.00149	222	16	2844	353	692	142	222	16
B1-10	432	0.260	0.17954	0.00379	0.07619	0.00122	1.88605	0.06211	0.05397	0.00108	1064	21	1100	29	1076	22	1100	29
B1-11	1587	0.962	0.11218	0.00217	0.07683	0.00069	1.18821	0.02430	0.03206	0.00081	685	13	1117	16	795	11	685	13
B1-12	648	0.435	0.05005	0.00143	0.07701	0.00968	0.53144	0.07879	0.01503	0.00055	315	9	1122	239	433	52	315	9
B1-13	805	0.483	0.03841	0.00088	0.06299	0.00300	0.33354	0.02185	0.01179	0.00023	243	5	708	94	292	17	243	5
B1-14	296	0.870	0.04224	0.00108	0.06799	0.00415	0.39594	0.03245	0.01286	0.00027	267	7	868	118	339	24	267	7
B1-15	600	0.338	0.04732	0.00087	0.05526	0.00048	0.36053	0.00718	0.01425	0.00030	298	5	423	18	313	5	298	5
B1-16	477	0.709	0.00557	0.00011	0.04996	0.00093	0.03839	0.00132	0.00165	0.00004	35.8	0.7	193	40	38	1	35.8	0.7
B1-17	322	0.305	0.04682	0.00103	0.06137	0.00183	0.39620	0.01883	0.01442	0.00028	295	6	652	59	339	14	295	6

(*continued on next page*)

Table 3 (*continued*)

Spot	U (ppm)	Th/U	U-Th-Pb ratios								Ages (Ma)						Inferred age (Ma)	
			206Pb/238U	1σ	207Pb/206Pb	1σ	207Pb/235U	1σ	208Pb/232Th	1σ	206Pb/238U	1σ	207Pb/206Pb	1σ	207Pb/235U	1σ		
B1-18	635	0.388	0.04759	0.00088	0.05250	0.00046	0.34444	0.00695	0.01372	0.00030	300	5	307	18	301	5	300	5
B1-19	161	0.581	0.06246	0.00118	0.05856	0.00059	0.50417	0.01146	0.01996	0.00047	391	7	551	20	415	8	391	7
B1-20	318	0.649	0.04676	0.00106	0.06057	0.00108	0.39039	0.01373	0.00848	0.00036	295	7	624	35	335	10	295	7
B1-21	338	0.917	0.04277	0.00081	0.05200	0.00050	0.30664	0.00673	0.01227	0.00028	270	5	285	20	272	5	270	5
B1-21-1	332	0.330	0.04466	0.00085	0.05274	0.00051	0.32471	0.00713	0.01451	0.00034	282	5	318	20	286	5	282	5
B1-22	27	0.403	0.00571	0.00025	0.07628	0.01296	0.06004	0.01250	0.00125	0.00025	37	2	1102	333	59	12	37	2
B1-23	4310	1.370	0.00378	0.00007	0.04707	0.00046	0.02455	0.00054	0.00115	0.00003	24.3	0.4	53	21	24.6	0.5	24.3	0.4
B1-23-1	2969	1.818	0.00405	0.00008	0.05138	0.00051	0.02867	0.00065	0.00129	0.00003	26.1	0.5	258	21	28.7	0.6	26.1	0.5
B1-24	646	0.180	0.07132	0.00135	0.05665	0.00051	0.55701	0.01143	0.02217	0.00056	444	8	478	18	450	7	444	8
B1-25	298	0.568	0.10781	0.00198	0.06740	0.00065	1.00177	0.02191	0.03704	0.00120	660	12	850	18	705	11	660	12
B1-26	164	0.787	0.00574	0.00013	0.06015	0.00233	0.04759	0.00275	0.00175	0.00006	36.9	0.8	609	77	47	3	36.9	0.8
B1-26.1	84	0.490	0.00596	0.00016	0.05267	0.00430	0.04326	0.00454	0.00183	0.00009	38	1	315	171	43	4	38	1
B1-27	195	0.613	0.00572	0.00013	0.05281	0.00199	0.04161	0.00236	0.00189	0.00005	36.8	0.8	321	79	41	2	36.8	0.8
B1-28	647	0.441	0.04634	0.00090	0.05510	0.00052	0.35203	0.00759	0.01402	0.00033	292	6	416	19	306	6	292	6

layer within the Tatunshan Formation in the latest Oligocene time as indicated by the youngest zircon U-Pb date (24 Ma), and slowly buried by successive Miocene strata to ~2 km depth (Teng, 1992). Such slow basinal burial diagenesis may have persisted until 12–8.5 Ma as the time the youngest Miocene strata in the northern Hsuehshan Range deposited, concurrent to when Taiwan Orogen started to develop (Lo and Yui, 1996; Teng, 1990; Huang et al., 2006).

The metamorphic conditions when cleavage was formed are constrained by the syn-kinematic growth of the corrensite-bearing mica porphyroblast (Chen et al., 2016). Corrensite is stable below ~250 °C (Cathelineau and Izquierdo, 1988), at the same time conspicuous muscovite presence emerging from illite starts from higher anchizone at no less than ~250 °C (Merriman and Peacor, 1999). Such assemblage, together with the maximum temperature inferred by RSCM data from nearby slate (246 ± 5 °C), suggest that the muscovite-corrensite porphyroblast and the host pressure solution seam were formed and deformed at the peak metamorphic state of ~250 °C, during ~6 to ~2.5 Ma as delineated by the *in-situ* $^{40}Ar/^{39}Ar$ laser microprobe dating results (Chen et al., 2016; Fig. 4C and D). The peak state interval overlaps with those determined from rocks of the retro wedge on the eastern border of the Central Range (Sandmann et al., 2015). By assuming a geothermal gradient of ~30 °C/km (the lower bound in integrated measurements by Yuan et al. (2009), from South China Sea marginal basins as contemporary tectonic equivalents of the Hsuehshan Range grabens), the depth of cleavage formation and peak metamorphic conditions was ~8 km, following a fast tectonic burial from ~2 km.

The subsequent exhumation and cooling were rapid as the rock ascending from ~8 km depth to earth surface was achieved within 2.5 million years. The exhumation pace was rather uniform as the apatite cooling age, 1.6 Ma at ~140 °C between 4 and 5 km deep (Wang, 2011), indicates a rock uplift rate of ~3 to 4 mm/yr both before and after 1.6 Ma.

4. Implications on Taiwan wedge kinematics

The time-temperature evolution deduced above reflects an intriguing history containing dramatic tectonic burial and exhumation, and the prolonged peak state residence in between. The particle trajectory exhibited by Sule Bridge pyroclastics (Fig. 5B) is not predicted in classical wedge model dominated by frontal accretion and self-similar growth (e.g. Barr et al., 1991), but closely tied to the basal accretion mechanism of wedge development (Kukowski et al., 2002; Glodny et al., 2005). Basal accretion has been highlighted as the major material influx pathway for the Taiwan Orogen based on thermochronologic and metamorphic investigations (Fuller et al., 2006; Beyssac et al., 2007), and one underplating domain where accretion took place is under the Hsuehshan Range in the pro-wedge (Simoes et al., 2007; Malavieille, 2010; Chen et al., 2011). The rapid tectonic burial preceding peak state recorded in the Sule Bridge pyroclastics therefore was acquired during underthrusting of the northern Hsuehshan Range rocks beneath the orogenic wedge to an underplating window starting at ~8 km depth if assuming a constant geothermal gradient of ~30 °C/km (Fig. 5).

The protracted dwelling at the peak state revealed in the thermal history has further implications on the growth of the orogenic wedge. Rocks in the northern Hsuehshan Range are among those first accreted into the orogenic wedge in the southward-propagating Taiwanese mountain belt, a fact confirmed by the temporal proximity between the onset of collision (Lin et al., 2003) and the start of cleavage formation as the oldest spot-fusion date at around 6 Ma (Chen et al., 2016). The accretion of the northern Hsuehshan Range nappes was succeeded by more underplated units beneath as plate convergence and mountain building continued during 6–2.5 Ma, while the later-accreted units must have entered the wedge through deeper underplating windows below since the former stayed at a rather constant depth indicated by the isothermal state during growth of pressure solution mineral

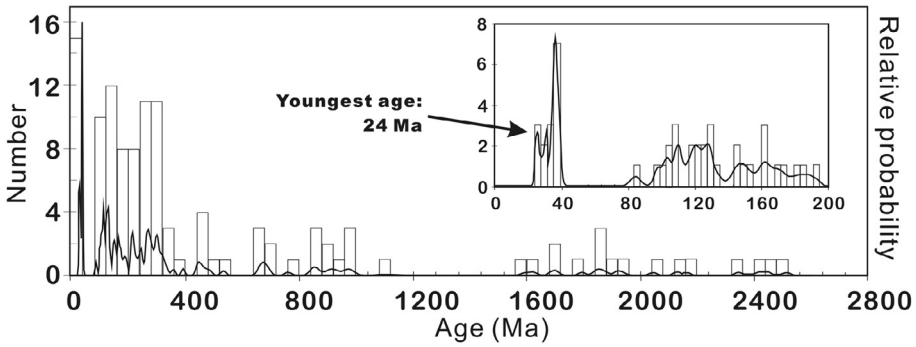

Fig. 3. Age distribution of zircons extracted from the Sule Bridge pyroclastics.

porphyroblasts. This suggests that the orogen grew with a deepening décollement which resulted in downward enlargement and thickening of the orogenic wedge, a manifestation of prolonged mountain root growth by vertical stacking of basal-accreted duplexes under the pro-wedge region (Fig. 5B). Such process operated on the northern Hsuehshan Range rocks since the inception of collision to ~2.5 Ma, equivalent to the incipient to full collisional stages in the temporal-spatial association of Taiwan (Shyu et al., 2005). Tectonic underplating thus was a major agent in crustal thickening of the Taiwan Orogen. It should be noted that in the topographic divide and retro-wedge of the Taiwan Orogen east of the Lishan Fault under the Backbone Range is another proposed site of basal accretion (Fig. 2; Beyssac et al., 2007; Malavieille, 2010) which may be linked in kinematics with the pro-wedge Hsuehshan underplating window studied here; episodic accretion been cyclical among the two basal accretion windows as well as frontal accretion (Gutscher et al., 1998) can not be ruled out and needs to be verified by new relevant data and observations. As no major exhumation is documented during ~6 to ~2.5 Ma for the underplated material, the pro-wedge of Taiwan by that time was likely to be kinematically decoupled: the shallower part of the wedge, the proto-wedge once overlying the northern Hsuehshan Range units, continued to grow and propagate foreland-ward by frontal accretion, meanwhile the lower part of the wedge including the studied northern Hsueshan Range nappes and further underplated units beneath were stacked towards depths (Fig. 5B), similar to those demonstrated by Kukowski et al. (2002). The section of wedge above the zone of underplating (2nd zone of underplating in Fig. 2) containing the underplated northern Hsuehshan Range nappes was subject to shortening and thickening which generated km-scale folding characteristics of the Hsuehshan Range (Clark et al., 1993; Chen et al., 2011), inducing minor amount of surface uplift while the basal-accreted units were kept isothermally at similar depths. Such folding might also contributed to the sustained growth of the dated muscovite-corrensite cleavage porphyroblast. The entire pro-wedge during ~6 to ~2.5 Ma was of lesser topography and relief than as of today, and might be submarine since sediments coming from the Taiwanese wedge only appeared around mid- to late Pliocene in the western foreland as the Chinshui Shale flysch deposits (Teng, 1990), signifying little erosion in the pro-wedge before ~3 Ma.

The pile of the underplated units beneath the Hsuehshan Range did not rise up until 2.5 Ma (the youngest mica porphyroblast spot fusion ages; Chen et al., 2016), and then underwent fast exhumation as constrained by apatite FT data. Combined with erosion, regional pop-up by reverse faulting on the Lishan and Chuchih faults (Clark et al., 1993) were likely the main contributors for such exhumation. This onset of rock uplift in the pro-wedge side postdates that in the retro wedge side as exhibited in a mylonite at the core of the Tananao Complex (Wang et al., 1998), suggesting different modes and rates of accretion and exhumation among pro- and retro-parts of the orogen. The ~2.5 Ma inception of rock uplift generally coincides with orogen-wide rapid exhumation across the Taiwan mountain belt (Lee et al., 2015; Hsu et al., 2016), which is also witnessed in detrital records of the surrounding basins (e.g. Teng, 1990; Kirstein et al., 2010), and led to exposures of metamorphic rocks as well as the build-up of high relief (e.g. Perrin et al., 2013). This evolution can be compared with that of the evolution of the Foreland in the western Alps when the thinned continental crust of the European plate was underthrusted beneath the internal Penninic nappes following continental subduction processes (Bonnet et al., 2007; Schwartz et al., 2017).

Our results are critical and have important implications for the general evolution of mountain belts. Most of them forms due to the subduction of a continental margin under another plate (continental or oceanic upper-plate), following closure of an oceanic domain. In this geodynamic setting, during continental subduction, the structures inherited from the former (rifting related) extensional tectonics play a major role. The existence of potential décollement levels and weaknesses in the crust (former faults, rheologic interfaces, weak layers in the sedimentary cover), will induce a specific accretionary behavior of the orogenic wedge. Such a mechanical behavior coupled with the effects of surface processes (erosion-sedimentation) will favor a combination of different accretionary processes acting at different levels in the wedge. In the pro-wedge, domains of basal accretion will coexist with frontal accretion resulting in a partitioning of deformation and specific kinematics, the main convergence being partitioned between horizontal and vertical paths of rock material. The Taiwan mountain belt is a present day example of the strong coupling between tectonic processes responsible for crustal thickening and surface processes responsible for rocks exhumation. Exhumation is currently concentrated in the domains where basal accretion is active, i.e. in the Hsuehshan Range and in the Backbone Range.

5. Conclusions

A complete rock thermal history from sedimentation through peak state deformation to exhumation is constrained for a meta-pyroclastics in the slate belt in northern Taiwan, the mature part of the arc-continent collision. Orogenic prograde metamorphism, as evidenced by RSCM peak temperature ~250 °C far exceeding basinal burial of ~2 km depth, was acquired during basal accretion when the northern Hsuehshan Range nappe containing the analyzed meta-pyroclastics underthrust beneath the now-eroded proto-wedge in latest Miocene. The nappe then resided at the peak thermal state during 6–2.5 Ma as revealed by *in-situ* $^{40}Ar/^{39}Ar$ laserprobe dating of co-genetic muscovite-corrensite growths along metamorphic foliation. Under continued plate convergence, more material was entering the wedge through this basal accretion mechanism; while the isothermal dwelling of the accreted northern Hsuehshan Range nappe suggests that tectonic underplating led to increases of décollement depths, hence downward thickening of the orogenic wedge and mountain root growth. Rapid exhumation commenced ~2.5 Ma, generally coeval to island-wide onset of fast rock uplift seen in thermochronological documentations, as well as the first arrival in the foreland basin of sediments derived from erosion of the Taiwan mountain belt. Basal accretion thus contributes significantly in the dynamics of the Taiwan arc-continent collision.

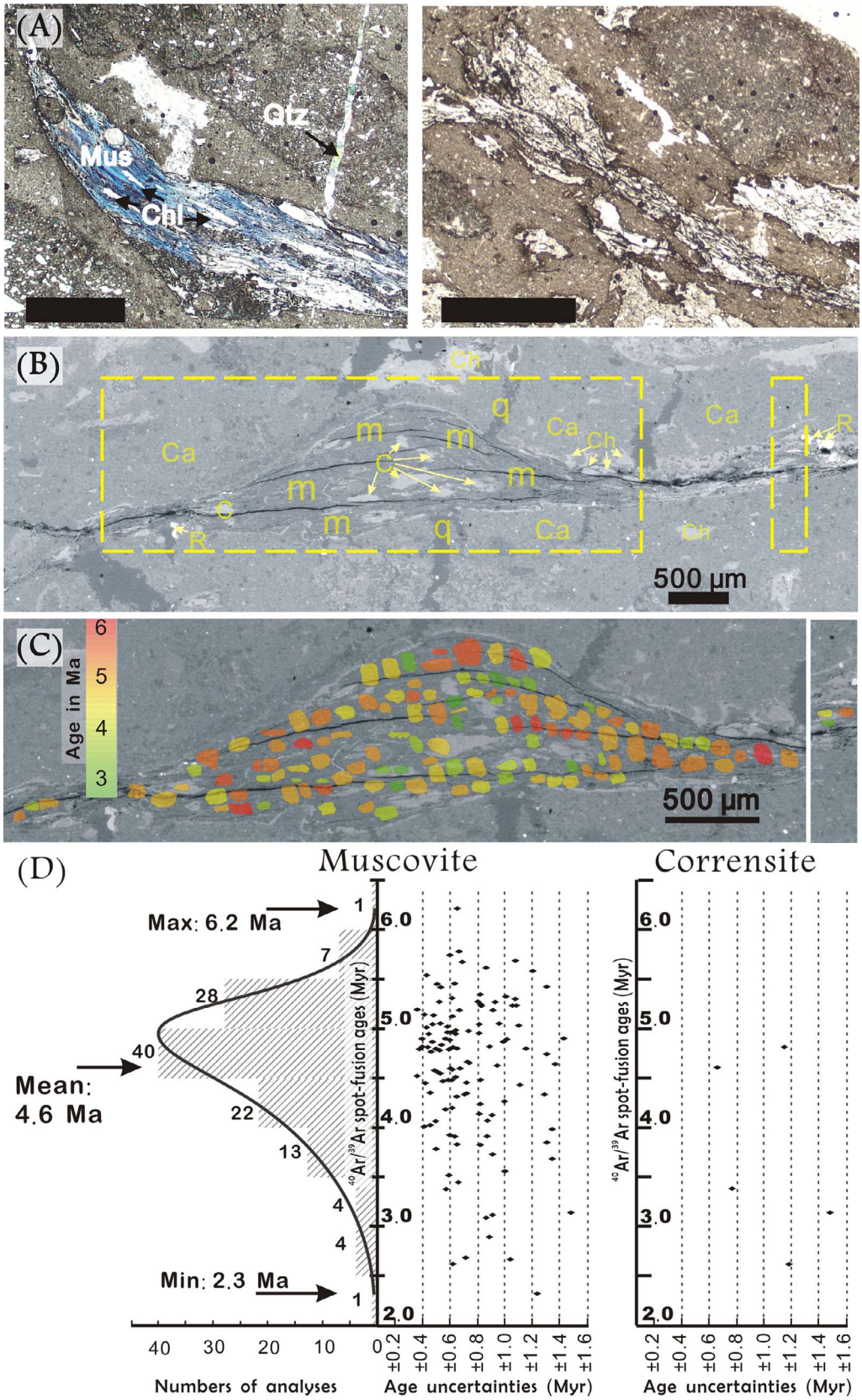

Fig. 4. (A) Photomicrographs of the Sule Bridge pyroclastics showing large mica porphyroblasts grown along pressure solution seams. Cross-polarized light; scale bar = 1 mm; Qtz: quartz; Mus: muscovite; Chl: chlorite/corrensite. (B) BSE image of the NCIH-B2 sample of the Sule Bridge pyroclastics, exhibiting mineral porphyroblasts along a pressure solution seam. Minerals: m: muscovite; c: corrensite; q: quartz; R: rutile; Ch: chlorite; Ca: calcite. Note the absence of simple shear deformation on porphyroblast shapes and neighboring grains. Areas shown in Fig. 4C are marked. (C): the *in-situ* $^{40}Ar/^{39}Ar$ laser microprobe dating results over BSE image. (D): $^{40}Ar/^{39}Ar$ laser microprobe ages plotted against age uncertainties (2σ) for results from muscovite and corrensite separately. Age data from Chen et al. (2016).

Acknowledgements

CTC wishes to acknowledge Tzen-Fu Yu, Hao-Tsu Chu, Olivier Beyssac, Martine Simoes, and Jian-Cheng Lee for their helpful discussions on the analytical techniques and Taiwan wedge kinematics. Sun-Lin Chung kindly facilitated zircon U-Pb analysis, and Jiin-Jyr Shyu for micro-Raman analysis. Constructive comments from Editors Mei-Fu Zhou and Michel Faure, and Giancarlo Molli and an anonymous

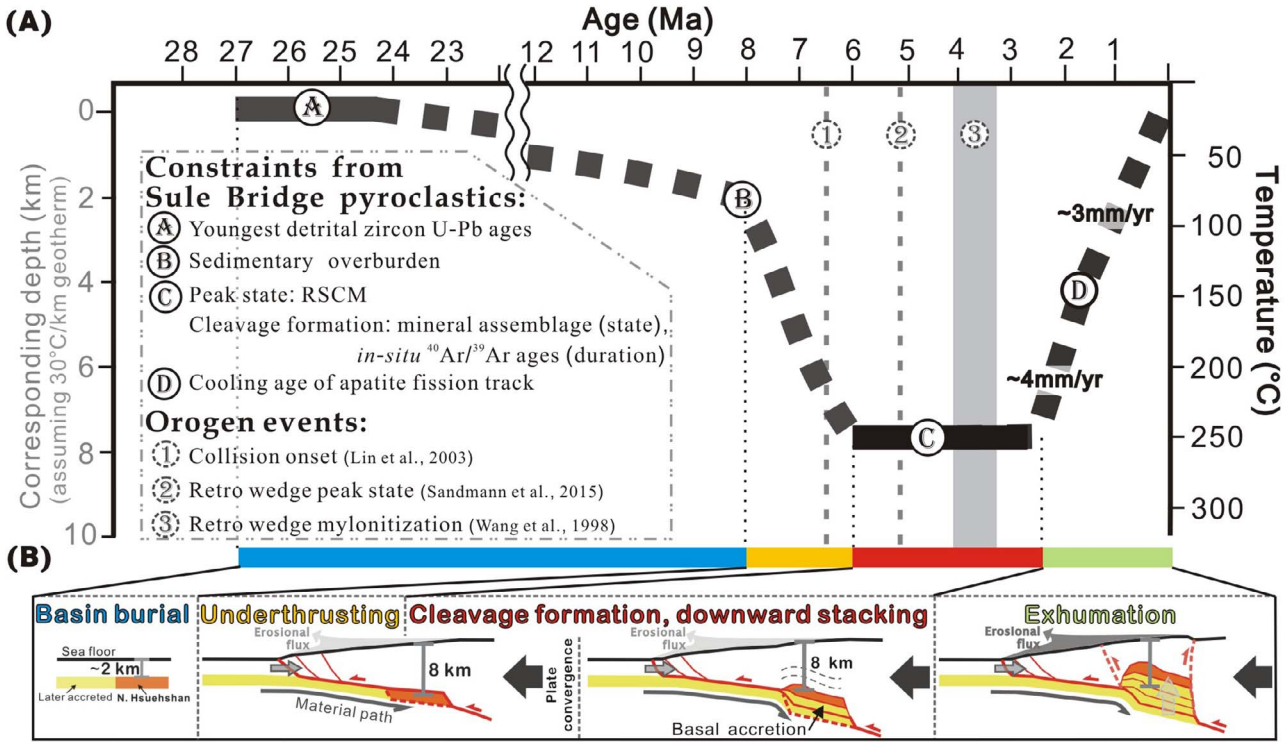

Fig. 5. (A) Time-temperature path of the Sule Bridge pyroclastics. (B) Proposed tectonic evolution of the northern Hsuehshan Range as constrained by metamorphic and chronologic data acquired from the Sule Bridge pyroclastics. The schematic sections correspond to the evolution of the second domain of underplating illustrated in the Fig. 2.

reviewer are deeply appreciated. This work was financially supported by Ministry of Science and Technology, Taiwan, R.O.C., under grant numbers: 106-2119-M-008-023 (C.-T. Chen), 105-2116-M-001-019 and 106-2116-M-001-020 (Y.-C. Chan), 102-2116-M-002-027-MY3 and 105-2811-M-002-123 and 106-2116-M-002-017 (C.-H. Lo), 105-2116-M-002-016 and 106-2116-M-002-016 (C.-Y. Lu), and National Central University grants to C.-T. Chen. This is Institute of Earth Sciences, Academia Sinica Contribution No. IESAS2176.

References

Barr, T.D., Dahlen, F.A., McPhail, D.C., 1991. Brittle frictional mountain building 3: low-grade metamorphism. J. Geophys. Res. 96-B6, 10319–10338.
Beyssac, O., Goffé, B., Chopin, C., Rouzaud, J.N., 2002. Raman spectra of carbonaceous material in metasediments: a new geothermometer. J. Metamorph. Geol. 20, 859–871.
Beyssac, O., Goffé, B., Petitet, J.-P., Froigneux, E., Moreau, M., Rouzaud, J.-N., 2003. On the characterization of disordered and heterogeneous carbonaceous materials by Raman spectroscopy. Spectrochim. Acta Part A Mol. Biomol. Spectrosc. 59, 2267–2276.
Beyssac, O., Simoes, M., Avouac, J.-P., Farley, K.A., Chen, Y.-G., Chan, Y.-C., Goffe, B., 2007. Late Cenozoic metamorphic evolution and exhumation of Taiwan. Tectonics 26, TC6001.
Bonnet, C., Malavieille, J., Mosar, J., 2007. Interactions between tectonics, erosion, and sedimentation during the recent evolution of the Alpine orogen: analogue modeling insights. Tectonics 26, TC6016.
Brown, D., Alvarez-Marron, J., Schimmel, M., Wu, Y.-M., Camanni, G., 2012. The structure and kinematics of central Taiwan mountain belt derived from geological and seismicity data. Tectonics 31, TC5013.
Byrne, T., Chan, Y.-C., Rau, R.-J., Lu, C.-Y., Lee, Y.-H., Wang, Y.-J., 2011. The arc-continent collision in Taiwan. In: Brown, D., Ryan, P. (Eds.), Arc-continent collision: the making of an orogen, Frontiers in earth sciences. Springer, Heidelberg, pp. 211–243.
Cathelineau, M., Izquierdo, G., 1988. Temperature-composition relationships of authigenic micaceous minerals in the Los Azufres geothermal system. Contrib. Miner. Petrol. 100, 418–428.
Chan, Y.-C., Crespi, J.M., Hodges, K.V., 2000. Dating cleavage formation in slates and phyllites with the $^{40}Ar/^{39}Ar$ laser microprobe: an example from the western New England Appalachians, USA. Terra Nova 12, 264–271.
Chang, L.S., 1973. A biostratigraphic study of the so-called Slate Formation in Taiwan based on smaller foraminifera: III. Sankuang-Hsiuluan area along the upper courses of the Tanshuiho and the Yulochi. Proc. Geol. Soc. China 20, 69–84.
Chen, C.-T., Chan, Y.-C., Lu, C.-Y., Simoes, M., Beyssac, O., 2011. Nappe structure revealed by thermal constraints in the Taiwan metamorphic belt. Terra Nova 23, 85–91.
Chen, C.-T., Lee, J.-C., Chan, Y.-C., Lu, C.-Y., Teng, L.S., 2014. Elucidating the geometry of the active Shanchiao Fault in the Taipei metropolis, northern Taiwan, and the re-activation relationship with preexisting orogen structures. Tectonics 33, 2400–2418.
Chen, C.-T., Chan, Y.-C., Lo, C.-H., Lu, C.-Y., 2016. Growth of mica porphyroblast under low-grade metamorphism – a Taiwanese case using *in-situ* $^{40}Ar/^{39}Ar$ laser microprobe analyses. J. Struct. Geol. 92, 1–11.
Chi, W.-R., Namson, J., Suppe, J., 1981. Stratigraphic record of plate interactions in the Coastal Range of eastern Taiwan. Geol. Soc. China Memoir 4, 155–194.
Chiu, H.-Y., Chung, S.-L., Wu, F.-Y., Liu, D., Liang, Y.-H., Lin, I.-J., Lizuka, Y., Xie, L.-W., Wang, Y., Chu, M.-F., 2009. Zircon U-Pb and Hf isotopic constraints from eastern Transhimalayan batholiths on the precollisional magmatic and tectonic evolution in southern Tibet. Tectonophysics 477, 3–19.
Chung, S.-L., Sun, S.-S., Tu, K., Chen, C.-H., Lee, C.-Y., 1994. Late Cenozoic basaltic volcanism around the Taiwan Strait, SE China: product of lithosphere -asthenosphere interaction during continental extension. Chem. Geol. 112, 1–20.
Clark, M.B., Fisher, D.M., Lu, C.-Y., Chen, C.-H., 1993. Kinematic analyses of the Hsueshan Range, Taiwan: a large-scale pop-up structure. Tectonics 12, 205–217.
Ernst, W.G., Jahn, B.M., 1987. Crustal accretion and metamorphism in Taiwan, a post-Palaeozoic mobile belt. Philos. Trans. R. Soc. Lond. A 321, 129–161.
Fuller, C.W., Willett, S.D., Fisher, D., Lu, C.-Y., 2006. A thermomechnical wedge model of Taiwan constrained by fission-track thermochronometry. Tectonophysics 425, 1–24.
Glodny, J., Lohrmann, J., Echtler, H., Gräfe, K., Seifert, W., Collao, S., Figueroa, O., 2005. Internal dynamics of a paleoaccretionary wedge: insights from combined isotope tectonochronology and sandbox modeling of the South-Central Chilean forearc. Earth Planet. Sci. Lett. 231, 23–39.
Gutscher, M.-A., Kukowski, N., Malavieille, J., Lallemand, S., 1998. Episodic imbricate thrusting and underplating: analog experiments and mechanical analysis applied to the Alaskan Accretionary Wedge. J. Geophys. Res. 103, 10161–10176.
Harrison, T.M., Celerier, J., Aikman, A.B., Hermann, J., Heizler, M.T., 2009. Diffusion of ^{40}Ar in muscovite. Geochim. Cosmochim. Acta 73, 1039–1051.
Hsu, W.-H., Byrne, T.B., Ouimet, W., Lee, Y.-H., Chen, Y.-G., van Soest, M., Hodges, K., 2016. Pleistocene onset of rapid, punctuated exhumation in the eastern Central Range of the Taiwan orogenic belt. Geology 44, 719–722.
Huang, C.-Y., Yuan, P.B., Tsao, S.-J., 2006. Temporal and spatial records of active arc-continent collision in Taiwan: a synthesis. Geol. Soc. Am. Bull. 118, 274–288.
Huang, T.-Y., Gung, Y., Kuo, B.-Y., Chiao, L.-Y., Chen, Y.-N., 2015. Layered deformation in the Taiwan orogen. Science 349, 720–723.
Huerta, A.D., Royden, L.H., Hodges, K.V., 1999. The effects of accretion, erosion and radiogenic heat on the metamorphic evolution of collisional orogens. J. Metamorph. Geol. 17, 349–366.
King, R.L., Bebout, G.E., Kobayashi, K., Nakamura, E., van der Klauw, S.N.G.C., 2004. Ultrahigh-pressure metabasaltic garnets as probes into deep subduction zone chemical cycling. Geochem. Geophys. Geosyst. 5, Q12J14.
Kirstein, L.A., Fellin, M.G., Willett, S.D., Carter, A., Chen, Y.-G., Garver, J.I., Lee, D.-C., 2010. Pliocene onset of rapid exhumation in Taiwan during arc-continent collision:

new insights from detrital thermochronometry. Basin Res. 22, 270–285.
Konstantinovskaia, E., Malavieille, J., 2005. Erosion and exhumation in accretionary orogens: experimental and geological approaches. Geochem. Geophys. Geosyst. 6, Q02006.
Kukowski, N., Lallemand, S.E., Malavieille, J., Gutscher, M.A., Reston, T.J., 2002. Mechanical decoupling and basal duplex for- mation observed in sandbox experiments with application to the Western Mediterranean Ridge accretionary complex. Mar. Geol. 186, 29–42.
Lahfid, A., Beyssac, O., Deville, E., Negro, F., Chopin, C., Goffe, B., 2010. Evolution of the Raman spectrum of carbonaceous material in low-grade metasediments of the Glarus Alps (Switzerland). Terra Nova 22, 354–360.
Lee, J.-C., Angelier, J., Chu, H.-T., 1997. Polyphase history and kinematics of a complex major fault zone in the northern Taiwan mountain belt: the Lishan Fault. Tectonophysics 274, 97–115.
Lee, Y.-H., Byrne, T., Wang, W.-H., Lo, W., Rau, R.-J., Lu, H.-Y., 2015. Simultaneous mountain building in the Taiwan orogenic belt. Geology 43–5, 451–454.
Lin, A.T., Watts, A.B., Hesselbo, S.P., 2003. Cenozoic stratigraphy and subsidence history of the South China Sea margin in the Taiwan region. Basin Res. 15, 453–478.
Liou, J.-G., Ernst, W.G., 1984. Summary of Phanerozoic metamorphism in Taiwan. Memoir Geol. Soc. China 6, 133–152.
Liu, T.-K., Hsieh, S., Chen, Y.-G., Chen, W.-S., 2001. Thermo-kinematic evolution of the Taiwan oblique-collision mountain belt as revealed by zircon fission track dating. Earth Planet. Sci. Lett. 186, 45–56.
Lo, C.-H., Onstott, T.C., 1995. Rejuvenation of K-Ar systems for minerals in the Taiwan Mountain Belt. Earth Planet. Sci. Lett. 131, 71–98.
Lo, C.-H., Yui, T.-F., 1996. $^{40}Ar/^{39}Ar$ dating of high-pressure rocks in the Tananao Basement Complex, Taiwan. J. Geol. Soc. China 39, 13–30.
Malavieille, J., 2010. Impact of erosion, sedimentation, and structural heritage on the structure and kinematics of orogenic wedges: analog models and case studies. GSA Today 20–1, 4–10.
Malavieille, J., Lallemand, S.E., Dominquez, S., Deschamps, A., Lu, C.-Y., Liu, C.-S., Schnurle, P., the ACT Scientific Crew, 2002. Arc-continent collision in Taiwan: New marine observation and tectonic evolution. Geol. Soc. Am. Spec. Pap. 358, 189–213.
Merriman, R.J., Peacor, D.R., 1999. Very low-grade metapelites: mineralogy, microfabrics and measuring reaction progress. In: Frey, M., Robinson, D. (Eds.), Low-Grade Metamorphism. Blackwell, Oxford, UK, pp. 10–60.
Passchier, C.W., Trouw, R.A.J., 2005. Microtectonics, second ed. Springer Verlag 366pp.
Perrin, C., Clemenzi, L., Malavieille, J., Molli, G., Taboada, A., Dominguez, S., 2013. Impact of erosion and décollements on large scale faulting and folding in orogenic wedges: analogue models and case studies. J. Geol. Soc., Lond. 170, 893–904.
Sandmann, S., Nagel, T.J., Froitzheim, N., Ustaszewski, K., Münker, C., 2015. Late Miocene to Early Pliocene blueschist from Taiwan and its exhumation via forearc extraction. Terra Nova 27, 285–291.
Schwartz, S., Gautheron, Audin, L., Dumont, T., Nomade, J., Barbarand, J., Pinna-Jamme, R., van der Beek, P., 2017. Foreland exhumation controlled by crustal thickening in the Western Alps. Geology 45, 139–142.
Shau, Y.-H., Peacor, D.R., Essene, E.J., 1990. Corrensite and mixed-layer chlorite/corrensite in metabasalt from northern Taiwan: TEM/AEM, EMPA, XRD, and optical studies. Contrib. Miner. Petrol. 105, 123–142.
Shyu, J.B.H., Sieh, K., Chen, Y.-G., 2005. Tandem suturing and disarticulation of the Taiwan orogen revealed by its neotectonic elements. Earth Planet. Sci. Lett. 233, 167–177.
Simoes, M., Avouac, J.P., Beyssac, O., Goffe, B., Farley, K.A., Chen, Y.-G., 2007. Mountain building in Taiwan: a thermokinematic model. J. Geophys. Res. 112, B11405.
Suppe, J., 1984. Kinematics of arc-continent collision, flipping of subduction and back-arc spreading near Taiwan. Memoir Geol. Soc. China 6, 21–33.
Teng, L.S., 1990. Geotectonic evolution of late Cenozoic arc-continent collision in Taiwan. Tectonophysics 183, 57–76.
Teng, L.S., 1992. Geotectonic evolution of Tertiary continental margin basins of Taiwan. Pet. Geol. Taiwan 27, 1–19.
Teng, L.S., Lin, A.T., 2004. Cenozoic tectonics of the China continental margin: insights from Taiwan. In: Malpas, J., Fletcher, C.J.N., Ali, J., Aitchison, J.C. (Eds.), Aspects of the Tectonic Evolution of China. Geological Society, London, Special Publications 226, pp. 313–332.
Wang, K.-L., Chung, S.-L., Lo, Y.-M., Lo, C.-H., Yang, H.-J., Shinjo, R., Lee, T.-Y., Wu, J.-C., Huang, S.-T., 2012. Age and geochemical characteristics of Paleogene basalts drilled from western Taiwan: records of initial rifting at the southern Eurasian continental margin. Lithos 155, 426–441.
Wang, P.-L., Lin, L.-H., Lo, C.-H., 1998. $^{40}Ar/^{39}Ar$ dating of mylonitization in the Tananao Schist, eastern Taiwan. J. Geol. Soc. China 41, 159–184.
Wang, H.-H., 2011. Exhumation history of the northern Hsuehshan Range and its tectonic implication (M.S. thesis). National Chung-Cheng University, Chiayi, Taiwan, pp. 46.
Wu, F.T., Liang, W.-T., Lee, J.-C., Benz, H., Villasenor, A., 2009. A model for the termination of the Ryukyu subduction zone against Taiwan: a junction of collision, subduction/separation, and subduction boundaries. J. Geophys. Res. 114, B07404.
Wu, F.T., Kuo-Chen, H., McIntosh, K.D., 2014. Subsurface imaging, TAIGER experiments and tectonic models of Taiwan. J. Asian Earth Sci. 90, 173–208.
Yang, H.-Y., Shau, Y.-H., 1988. Occurrence of pumpellyite-bearing basaltic tuffs in Hsuehshan Range. Proc. Geol. Soc. China 31, 24–32.
Yuan, Y., Zhu, W., Mi, L., Zhang, G., Hu, S., He, L., 2009. “Uniform geothermal gradient” and heat flow in the Qiongdongnan and Pearl River Mouth Basins of the South China Sea. Mar. Pet. Geol. 26, 1152–1162.
Yui, T.-F., Lu, C.-Y., Lo, C.-H., 1988. A speculative tectonic history of the Tananao Schist of Taiwan. Proc. Geol. Soc. China 31–2, 7–18.